Numerical simulation of nanoparticle acceleration in a Laval micronozzle with subsequent deceleration in a wall compression layer

S.P. Kiselev and V.P. Kiselev
Khristianovich Institute of Theoretical and Applied Mechanics,
Novosibirsk 630090, Russia
E-mail: kiselev@itam.nsc.ru

Abstract

In the present article, simulation data for copper nanoparticles undergoing acceleration in a Laval micronozzle and then experiencing deceleration in a wall compression layer are reported. It is shown that, at the expense of reduced dimensions of the nozzle and reduced nozzle exit - to - obstacle separation, a sufficiently high impact velocity of nanoparticles can be achieved, allowing the nanoparticles to stick to the obstacle surface with the formation of a coating, like it occurs in a cold spray process. A size effect manifested as the dependence of nanoparticle impact velocity on the problem geometric sizes is revealed, related with the presence of a characteristic relaxation time in the problem.

Key words: numerical simulation, nanoparticles, micronozzle, cold spray technology, supersonic jet, shock wave.

1. INTRODUCTION

Presently, the cold spray technology has found wide application [1]. In a cold spray process, microparticles are accelerated in a supersonic Laval nozzle to a velocity of a few hundred meters per second. After the microparticles impinge onto the obstacle, their kinetic energy goes into the internal energy, allowing the microparticles to stick to the obstacle with the formation of a coating. In front of the obstacle, a reflected shock wave forms, this shock wave envelops a gas compression layer formed near the obstacle surface. In the compression layer, the microparticles experience deceleration, so that their impact velocity decreases. On decreasing the particle size, the rate of particle deceleration in the compression layer increases. If the impact velocity decreases below some critical value, then no coating deposition becomes possible. In [2] we showed, by means of numerical simulations, that, for the size of particles impinging onto the surface to be decreased, one has to reduce the dimensions of the Laval nozzle. It can be expected that, with the Laval-nozzle dimensions substantially reduced, it would then become possible to scale down the size of the particles used in the spray process so that to bring this size to the nanometer range. In the present study, we numerically simulated the acceleration of nanoparticles in a Laval nozzle followed with their subsequent deceleration in a wall compression layer. Our purpose was to examine the possibility of nanoparticle spraying from a Laval micronozzle.

2. SECTIONS: MATHEMATICAL STATEMENT OF THE PROBLEM.

Consider an axisymmetric two-phase gas-particle jet in the domain shown in Fig. 1. The domain comprises an axisymmetric Laval nozzle ($0 < z < Z_b$) and the region between the nozzle and the obstacle onto which the jet impinges ($Z_b < z < Z_w$). In front of the wall, there forms a reflected shock wave in which the jet undergoes deceleration to subsequently become propagating in the normal direction along the wall.

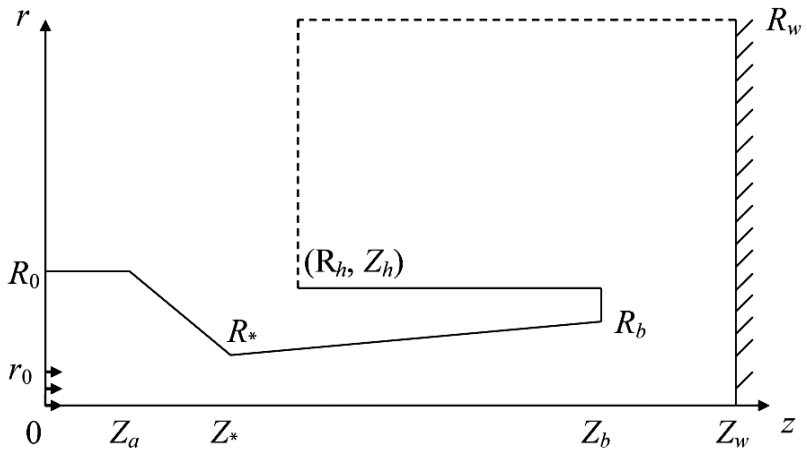

Fig. 1. Computational domain. The nozzle contour is shown with the solid line.

At the inlet to the nozzle (z = 0), the gas pressure p_0 and the gas temperature T_1^0 are set. The gas flow $j_g = \rho u$ and the mass rate of this flow $Q_g = j_g \cdot S$, both dependent on problem parameters, are to be determined as the solution of the problem. The flux of the particles $j_p = m_2^0 \rho_p u_2^0$ and the mass rate of their flow $Q_p = j_p \cdot S_0$ are defined by the parameters m_2^0 and u_2^0 specified at the nozzle inlet. Here, ρ and u are the gas density and the gas velocity, ρ_p and u_2 are the density and velocity of the particles, $m_2 = \pi d_p^3 n / 6$ is the volume concentration of the particles, d_p and n are the diameter and the number concentration of the particles, and S is the nozzle cross-sectional area. In the present simulations, the gas was air, and the particles were copper particles.

The copper particles impinge onto the wall under conditions with a characteristic gas flow velocity u ≈ 550 ÷ 600 m/s [1]. Values $R_* \approx 25$ μm and $v \approx 1.5 \cdot 10^{-5}$ m^2/s adopted for the nozzle radius and for the kinematic viscosity translate into a value $\mathrm{Re}_j = u \cdot R_* / v \approx 1.5 \cdot 10^3$ for the jet Reynolds number, this value being lower than the critical Reynolds number $R_* \approx 5 \cdot 10^3$ for laminar-turbulent transition in a pipe flow [3]. That is why the nozzle flow is everywhere laminar, obeying Navier - Stokes equations with forces due to gas-particle interaction introduced into the right-hand sides of the equations [4-6]:

$$\frac{\partial \varphi}{\partial t} + \frac{\partial F}{\partial z} + \frac{\partial G}{\partial r} + H = 0,$$

$$p = (\gamma - 1)\rho E, \;\; e = \rho(E + (u^2 + v^2)/2), \;\; E = C_v T_1 \,,$$

$$\phi = \begin{pmatrix} \rho \\ \rho u \\ \rho v \\ e \end{pmatrix}, \; F = \begin{pmatrix} \rho u \\ \rho u^2 + p - \tau_{zz} \\ \rho uv - \tau_{zr} \\ u(e+p) - (u\tau_{zz} + v\tau_{zr} + \dot{q}_z) \end{pmatrix}, \; G = \begin{pmatrix} \rho v \\ \rho uv - \tau_{zr} \\ \rho v^2 + p - \tau_{rr} \\ v(e+p) - (u\tau_{zr} + v\tau_{rr} + \dot{q}_r) \end{pmatrix}, \quad (1)$$

$$H = \begin{pmatrix} \rho v / r \\ (\rho uv - \tau_{zr})/r - F_z \\ (\rho v^2 + \tau_{\theta\theta} - \tau_{rr})/r - F_r \\ (v(e+p) - u\tau_{zr} - v\tau_{rr} - \dot{q}_r)/r - uF_z - vF_r - \Phi \end{pmatrix},$$

$$\tau_{zz} = 2\mu\left(\frac{\partial u}{\partial z} - \frac{1}{3}D\right), \; \tau_{rr} = 2\mu\left(\frac{\partial v}{\partial r} - \frac{1}{3}D\right), \; \tau_{\theta\theta} = 2\mu\left(\frac{v}{r} - \frac{1}{3}D\right), \; \tau_{zr} = \mu\left(\frac{\partial u}{\partial r} + \frac{\partial v}{\partial z}\right),$$

$$\dot{q}_z = \lambda \frac{\partial T_1}{\partial z},\ \dot{q}_r = \lambda \frac{\partial T_1}{\partial r},\ D = \frac{\partial u}{\partial z} + \frac{\partial v}{\partial r} + \frac{v}{r},\quad \mu = C_1 \frac{T_1^{3/2}}{T_1 + C_2}\cdot$$

In Eqs. (1), the designations are as follows: u, v, ρ, p, E, and T_1 are the velocity along the z-axis, the velocity along the r-axis, the density, the pressure, the internal energy, and the gas temperature; F_z and F_r are the force components due to the inter-phase gas - particle interaction; Φ is the flux of energy from the particles to the gas flow; τ_{zz}, τ_{rr}, $\tau_{\theta\theta}$, and τ_{zr} are the components of the gas viscous stress tensor; $\dot{q}_z$ and $\dot{q}_r$ are the components of the heat flow vector; and C_v = 732 J/(kg·K) is the specific heat of air at constant volume. The dynamic gas viscosity μ can be expressed the Sutherland formula with coefficients C_1 and C_2, for these coefficients, values $C_1 = 1.458 \cdot 10^{-6}\ \mathrm{Pa \cdot sec/\sqrt{K}}$ and C_2 = 110.4 K were adopted. The heat conductivity λ was calculated by the formula λ = Pr/ (C_p μ), where Pr = 0.72 is the Prandtl number, $C_p = \gamma C_v$ is the specific heat at constant pressure, and γ is the air adiabatic exponent.

We assume here that the volume concentration of the particles is low $m_2 \approx 10^{-4} - 10^{-5}$, so that inter-particle collisions may be neglected. In the latter case, the particle motion can be predicted using the collisionless kinetic equation [4 - 6]:

$$\frac{\partial f}{\partial t} + u_2 \frac{\partial f}{\partial z} + v_2 \frac{\partial f}{\partial r} + \frac{\partial f_z f}{\partial u_2} + \frac{\partial f_r f}{\partial v_2} + \frac{\partial q f}{\partial T_2} = 0,$$

$$f = f(t, z, r, u_2, v_2, T_2),\ m_1 + m_2 = 1,$$

$$n = \int f\, dV,\ m_2 = \int V_p f\, dV, dV = d u_2\, d v_2\, d T_2,\ V_p = \pi d_p^3 / 6,$$

$$F_z = -\int m_p f_z f\, dV,\ F_r = -\int m_p f_r f\, dV, \tag{2}$$

$$\Phi = \int m_p ((u - u_2) f_z + (v - v_2) f_r - c_s q) f\, dV,\ m_p = \rho_p V_p,$$

$$f_z = (u - u_2)/\tau,\ f_r = (v - v_2)/\tau,\ q = \pi \lambda d_p\, Nu (T_1 - T_2)/C_s m_p,$$

$$1/\tau = 3\mu \,\mathrm{Re}\, C_d / \rho_p d_p^2,\ Nu = 2 + 0.6\sqrt{\mathrm{Re}}\,\mathrm{Pr}^{0.33},$$

$$\mathrm{Re}_{12} = \rho |v - v_2| d_p / \mu,\ M_{12} = |v - v_2| / c,\ c = \sqrt{\gamma p / \rho}\ .$$

In (2), the following designations were adopted: f is the distribution function for the particles; n, m_2, and m_1 are the number concentration of particles, the volume concentration of particles, and the volume concentration of the gas; u_2, v_2, T_2, d_p, V_p, ρ_p, m_p, and C_s are the particle velocity along the z-axis, the particle velocity along the r-axis, the temperature, the diameter, the density, the mass, and the heat capacity of a single particle; f_z and f_r are the components of the force that acts from the side of the gas on a unit-mass particle along the z - and r-axes; q is the heat flow from the gas to the particle; and Nu, Re_{12}, and M_{12} are the Nusselt, Reynolds, and Mach number for the flow past a single particle.

In calculating the drag force for the nanoparticles, the effects due to gas rarefaction become substantial. In calculating the drag coefficient C_d for the drag force of a particle, we used the Henderson formula [7]. This formula, applicable in a broad range of flow quantities in the vicinity of the particle, from Knudsen to continuum flow, has the form

$$C_d = \begin{cases} C_{d1}, \quad \mathrm{M}_{12} < 1, \\ C_{d1}(\mathrm{M}_{12}=1) + \dfrac{4}{3}\left(\mathrm{M}_{12}-1\right)\left[C_{d2}\left(\mathrm{M}_{12}=1.75\right) - C_{d1}(\mathrm{M}_{12}=1)\right], \quad 1 < \mathrm{M}_{12} < 1.75, \\ C_{d2}, \quad \mathrm{M}_{12} > 1.75 \end{cases}$$

$$C_{d1} = \frac{24}{\left[\mathrm{Re}_{12} + S\left(4.33 + f_1 f_{e1}\right)\right]} + f_{e2}\left(f_2 + 0.1\mathrm{M}_{12}^2 + 0.2\mathrm{M}_{12}^8\right) + f_{e3}$$

$$f_1 = \frac{3.65 - 1.53T_2/T_1}{1 + 0.353T_2/T_1}, \; f_{e1} = \exp\left(-\frac{0.247\,\mathrm{Re}_{12}}{S}\right), \; S = \sqrt{\frac{\gamma}{2}}\mathrm{M}_{12}$$

$$f_2 = \frac{4.5 + 0.38\left(0.03\,\mathrm{Re}_{12} + 0.48\sqrt{\mathrm{Re}_{12}}\right)}{1 + 0.3\,\mathrm{Re}_{12} + 0.48\sqrt{\mathrm{Re}_{12}}}, \; f_{e2} = \exp\left(-\frac{0.5\mathrm{M}_{12}}{\sqrt{\mathrm{Re}_{12}}}\right) \tag{3}$$

$$f_{e3} = 0.6 \cdot \left[1 - \exp\left(-\frac{\mathrm{M}_{12}}{\mathrm{Re}_{12}}\right)\right] \cdot S, \; g_1 = \frac{2 + 2/S^2 + 1.058\dfrac{T_2}{T_1 S} - \dfrac{1}{S^4}}{1 + 1.86\dfrac{\mathrm{M}_{12}}{\mathrm{Re}_{12}}}$$

$$C_{d2} = 0.9 + \frac{0.34}{\mathrm{M}_{12}^2} + 1.86\frac{\mathrm{M}_{12}}{\mathrm{Re}_{12}} g_1$$

The numerical procedure for system (1, 2) and the verification procedure for the solution were described at length elsewhere [5, 6]. The equations for the gas-particle system were solved numerically using the Euler - Lagrange method. Gas equations (1) were solved in a curvilinear coordinate system on a uniform Euler grid with the help of the Rusanov finite-difference scheme of third-order accuracy [8]. Particle equations (2) were solved by the Lagrange method. The region seeded with the particles was divided into cells, which in the axisymmetric case were rings with cross-sections shaped as rectangles. The motion of the centers of the particle cells was predicted using ordinary differential equations for particle trajectories; these trajectories coincided with the characteristics of the kinetic equation. In calculating the inter-phase force, linear interpolation of particle quantities onto the gas Euler grid and linear interpolation of gas-flow quantities onto the Lagrange particle cells were used.

To calculate the gas flow dusted with particles, we used the relaxation method. At the nozzle wall, no-slip condition for the gas flow and elastic reflection condition for the particles were assumed. For the gas temperature, condition of zero derivative of temperature along the normal to the wall, which modeled the adiabatic-wall condition, was adopted. At the obstacle surface, no-slip condition for the gas flow was used, with all particles being absorbed there by the obstacle. At the jet axis, symmetry condition was used for the z-component of gas velocity, while the r-component of gas velocity was put equal to zero. For the particles, elastic reflection condition at the jet axis was adopted. The gas jet dusted with the particles emanated from the Laval nozzle into the region bounded by the obstacle surface and by an external boundary shown in Fig. 1 with a dashed line. At the outer boundary, «soft» boundary conditions in the form of zero derivatives of flow quantities were posed. The outer boundary of the region around the nozzle was located far enough from the nozzle so that to exclude the influence of the «soft» boundary conditions on the gas flow in the vicinity of the nozzle.

The initial conditions were set as a jump of pressure (in the supersonic part of the nozzle) from the inlet pressure p_0 to 1 atm. At the nozzle inlet (z = 0), constant values of gas (p_0, T_0) and particle quantities were maintained. After the decay of pressure discontinuity, the emerging waves were carried out from the nozzle with subsequent relaxation of the flow.

3. SECTIONS: CALCULATION DATA AND THEIR DISCUSSION.

We examined the acceleration of copper nanoparticles in three Laval micronozzles hereinafter referred to as micronozzles S(50), S(100), and S(200). The linear sizes in micronozzle S(100) were twice, and those in micronozzle S(200), four times larger than the linear sizes in micronozzle S(50). Consider first nanoparticle acceleration in micronozzle S(50). This micronozzle had the following dimensions: outlet diameter D_b = 50 μm (outlet radius $R_b = D_b / 2$), throat radius $R_* = R_b / 2$, nozzle length Z_b = 1 mm, subsonic length Z_* = 0.25 mm, inlet radius R_0 = 38 μm. The nozzle exit-to-wall separation was equal to the nozzle outlet diameter $Z_w - Z_b = D_b$. The copper nanoparticles of diameter d_p = 50 nm were injected into the flow at z = 0 uniformly over a circular region of radius r_0 = 30 μm (see Fig. 1). The velocity of injected particles was u_2^0 = 10 m/s, and their volume concentration $m_2^0 = 10^{-5}$. At the inlet to the nozzle, the pressure p_0 = 30 atm and the temperature T_0 = 500 K were set.

Figures 2 and 3 show the fields of Mach number, pressure, temperature, and particle concentration calculated for micronozzle S(50).

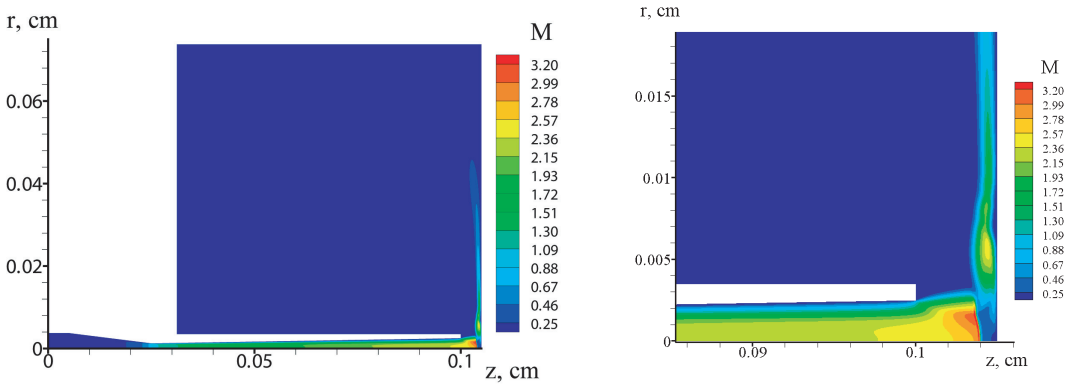

Fig. 2. Distribution of Mach number in micronozzle S(50) throughout the entire flow domain (*a*) and in the vicinity of the obstacle (*b*).

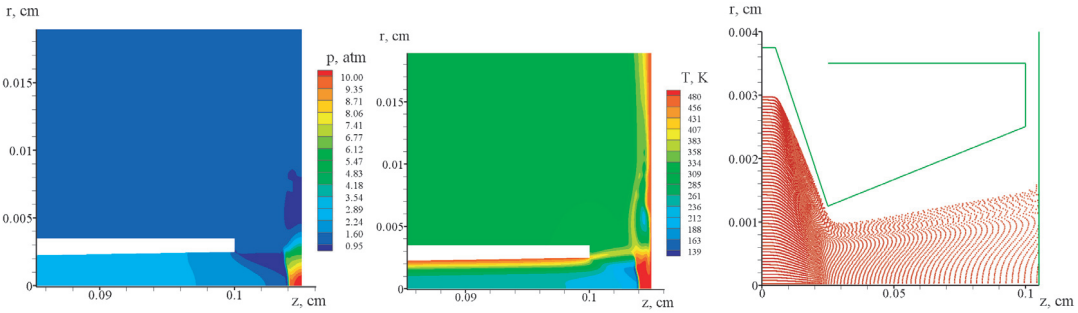

Fig. 3. Distribution of pressure (*a*) and temperature (*b*) in the vicinity of the obstacle. Distribution of nanoparticle concentration in micronozzle S(50) (*c*).

It follows from Figs. 2 and 3 that the gas accelerates in micronozzle S(50) to a supersonic velocity corresponding to the Mach number M ≈ 3 at the nozzle exit plane. Over the supersonic length, the gas flow is close to a quasi-one-dimensional flow. The effect due to viscosity becomes substantial in the boundary layer near the nozzle wall. Figure 4 shows the distribution of velocity and temperature at four cross-sections of the jet flow. The gas velocity and the boundary-layer thickness are seen to monotonically grow with the z-coordinate.

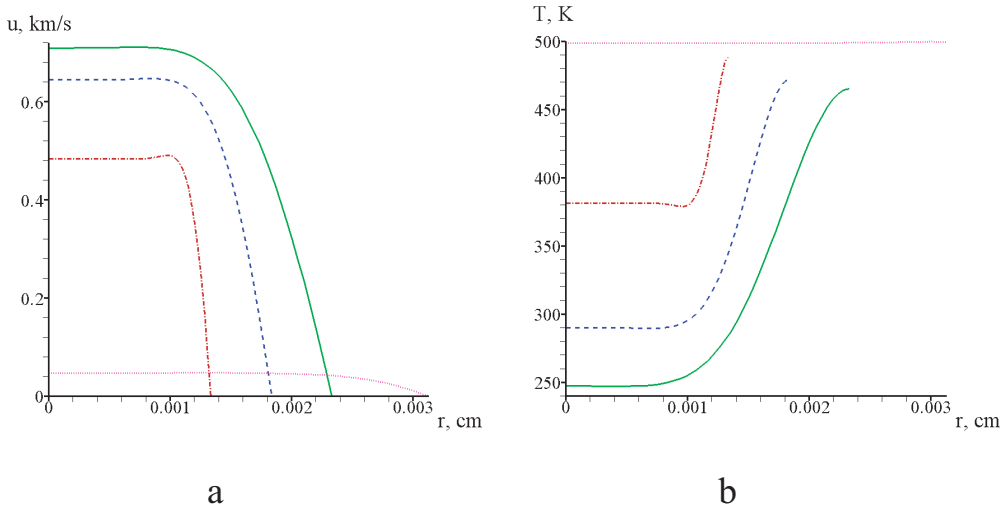

Fig. 4. Radial distribution of gas velocity u(r) (*a*) and gas temperature T(r) (*b*) at cross-sections z=0.1 mm (pink dots), z=0.3 mm (red dash-and-dot line), z=0.6 mm (blue dashed line), and z=0.9 mm (green solid line).

On the contrary, the gas temperature decreases monotonically as the internal gas energy transforms into the kinetic energy of gas and particle flow. The viscous force works to additionally heat the gas. That is why the maximum temperature is achieved near the wall, and the temperature decreases along the z-coordinate more slowly in the boundary layer.

Over the subsonic length, the gas jet suffers compression, and this results in some contraction of the nanoparticle jet, see Fig. 3 *c*. The jet contraction over the subsonic length is more pronounced than the jet expansion over the supersonic length, making the nanoparticle jet focusing. Thus, a proper choice of nozzle geometry allows one to achieve focusing of the nanoparticle jet. Note that the focusing is not violated in the region between the micronozzle and the obstacle. Figure 5 shows the distribution of gas velocity, gas temperature, particle velocity, and particle temperature along the jet axis.

In the micronozzle, the two-phase gas-particle jet undergoes simultaneous acceleration and cooling. The velocity and temperature of the nanoparticles there differ little from the velocity and temperature of the gas flow. As a result of the deceleration of the gas flow, a hot gas compression layer, enveloped from the left with a shock wave, forms near the obstacle. In this layer the nanoparticles undergo heating and deceleration. The velocity $u_2^* = u_2(Z_w)$ at which the nanoparticles impinge onto the obstacle will be called below the impact velocity. As it is seen from Fig. 5 *c* and *d*, the velocity u_2^* equals 530 m/s, the nanoparticle temperature being of order 400 K. This impact velocity value is close to the critical velocity of copper particles $u_* \approx 550 \div 600$ m/s [1] at which the particles begin sticking to the obstacle surface with the formation of a coating. Note the spatial oscillations of gas velocity and gas temperature at the front of the shock wave (see Fig. 5 *c* and *d*), which are typical of difference schemes of third-order accuracy [9]. These oscillations are seen not to affect the magnitude of the velocity and temperature of those nanoparticles which traverse the shock-wave front with preservation of their velocity and temperature.

The velocity and temperature of nanoparticles strongly depend on the air temperature T_0 at the inlet to the micronozzle. A 100-degree increase of T_0 results in that the impact velocity of nanoparticles increases to 605 m/s (Fig. 6).

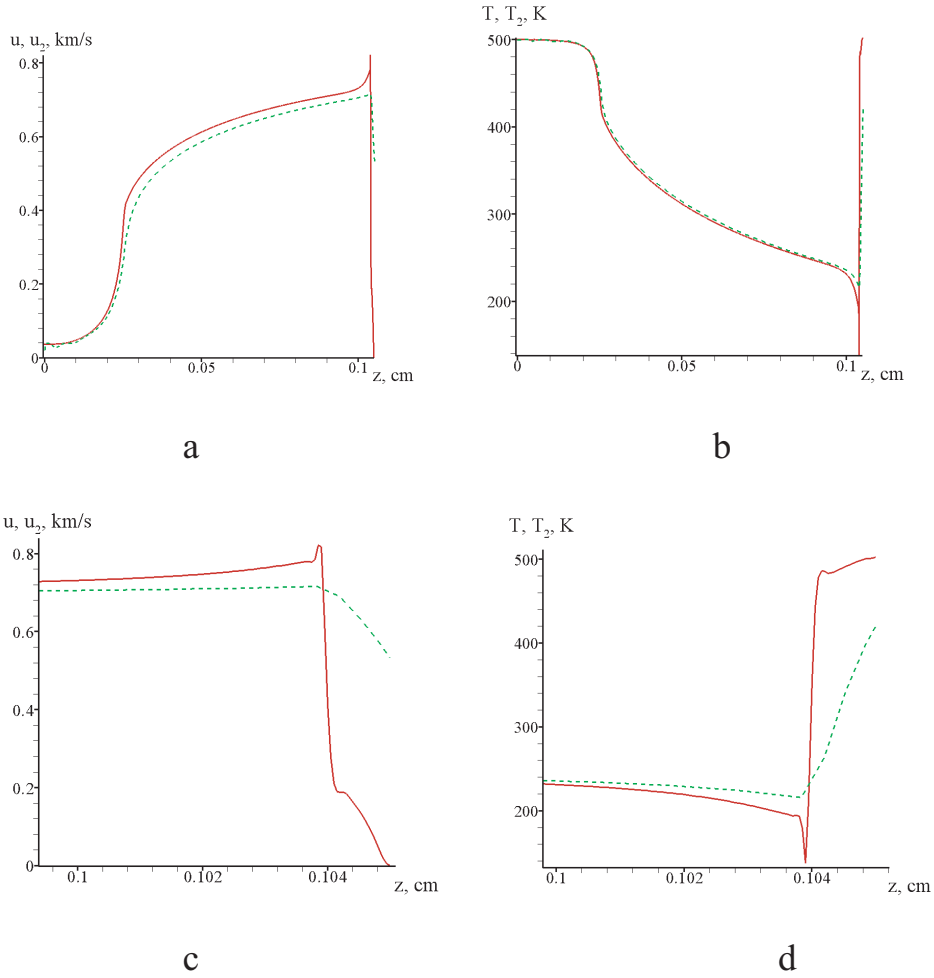

Fig. 5. Longitudinal distribution of gas velocity u(z) and particle velocity u_2(z) (*a*), and gas temperature T(z) and particle temperature T_2(z) (*b*), at the jet axis. Longitudinal distribution of u(z) and u_2(z) (*c*), and T(z) and T_2(z) (*d*), at the jet axis in the region between the nozzle exit and the obstacle. The red line in the figures shows the gas quantities, and the green dashed line shows the nanoparticle quantities.

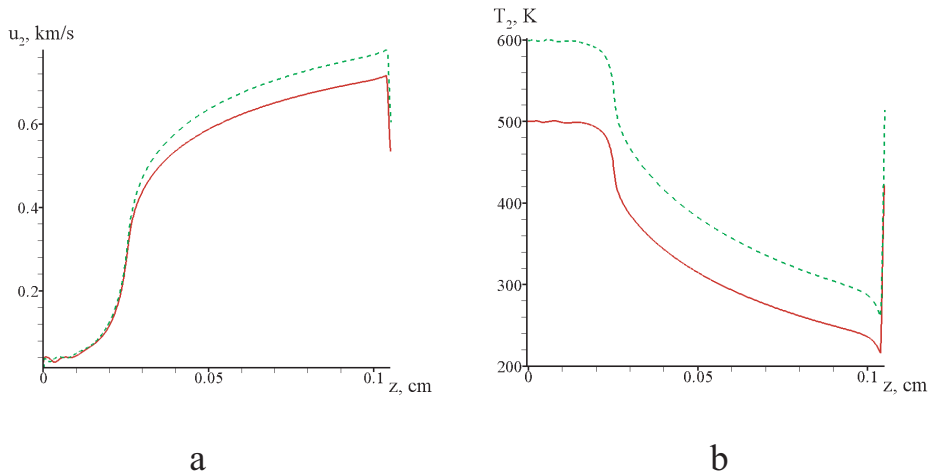

Fig. 6. Longitudinal distributions of particle velocity (*a*) and particle temperature (*b*) at the jet axis calculated for two values of T_0. The red solid line and the green dashed line refer respectively to T_0=500 K and T_0=600 K.

In this case, with the chosen micronozzle and carrier-flow parameters, sticking of copper nanoparticles to the surface with the formation of a coating is possible.

Consider now the calculation data for copper nanoparticles that undergo acceleration in micronozzle S(100) (Figs. 7 and 8). All linear dimensions in micronozzle S(100) were increased two-fold in comparison with micronozzle S(50). The outlet diameter for micronozzle S(100) was 100 μm, and the length of the micronozzle was 2 mm. The gas and particle quantities at the inlet to micronozzle S(100) were the same as in micronozzle S(50), except for the particle diameter, which was also increased two-fold, d_p = 100 nm.

The calculated gas and particle quantities in micronozzle S(100) (Figs. 7 and 8 *a*) differ little from the same gas (Figs. 2 and 3) and particle quantities (Fig. 5 *a*) in micronozzle S(50).

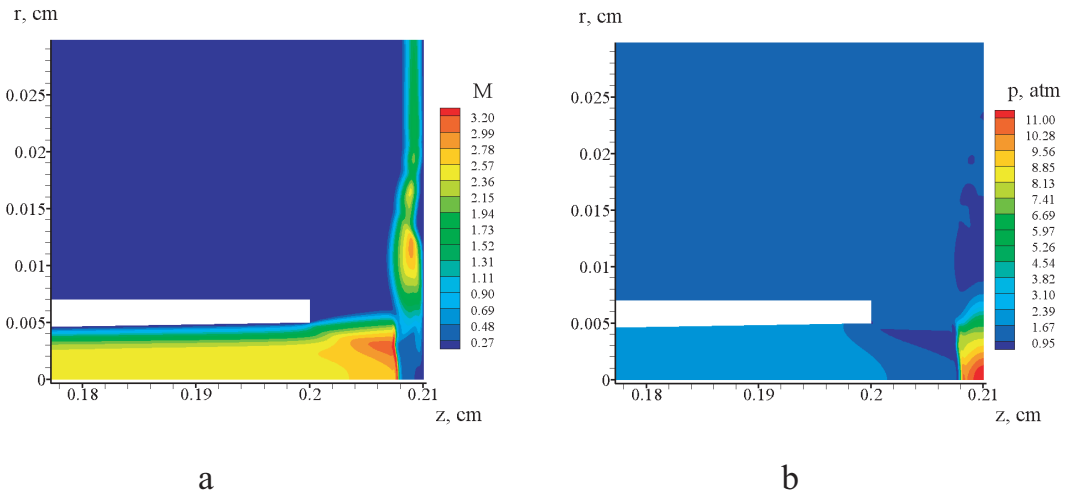

Fig. 7. Calculated Mach number (*a*) and pressure (*b*) in micronozzle S(100).

Figure 8 *a* shows the gas velocity and the particle velocity for nanoparticles of diameter d_p = 100 nm versus the z-coordinate.

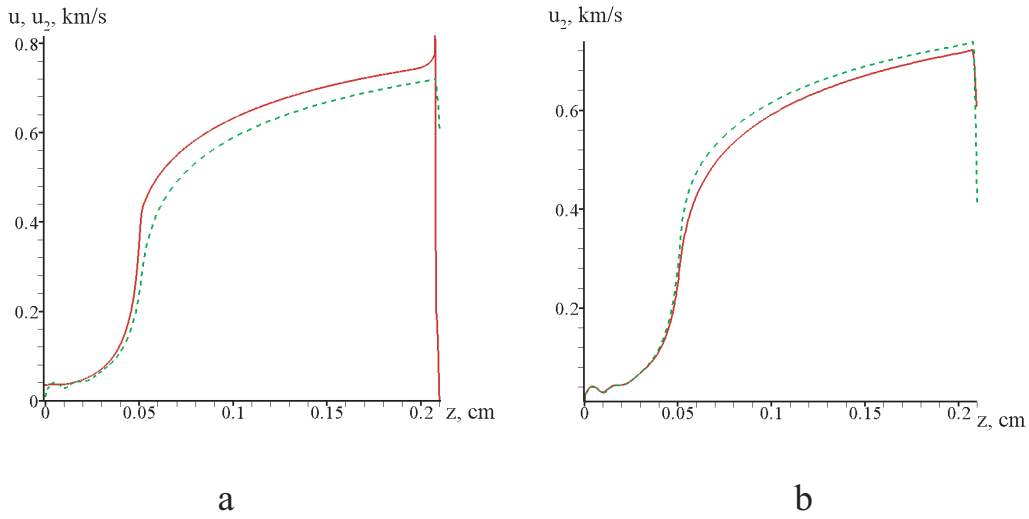

Fig. 8. Calculated gas velocity u(z) (*a*) and particle velocity u_2(z) (*b*) at the jet axis in micronozzle S(100). The particle diameter is d_p = 100 nm (red solid line) and d_p = 50 nm (green dashed line) in micronozzle S(100).

It is seen from Fig. 8 *a*, that the gas velocity and the particle velocity in the micronozzle have close values. In the compression layer the gas velocity vanishes at the obstacle surface, whereas the particle velocity changes moderately. The impact velocity of the nanoparticles is 570 m/s, this value being high enough for the formation of a coating.

Besides, we calculated the acceleration of nanoparticles of diameter d_p = 50 nm in micronozzle S(100). Figure 8 *b* shows the curves of $u_2(z)$ calculated for 50- and 100-nm diameter nanoparticles in micronozzle S(100). At the nozzle outlet, both particle velocities have close values. Yet, in the compression layer nanoparticles with d_p = 50 nm decelerate more strongly than nanoparticles with d_p = 100 nm. As a result, the impact velocity of nanoparticles with d_p = 50 nm, amounting to 370 m/s, turns out to be 200 m/s lower than that for nanoparticles with d_p = 100 nm. This value is insufficiently high for a coating to form. The main reason for the strong deceleration of nanoparticles with d_p = 50 nm in the compression layer is the two-fold increase of the compression-layer thickness in micronozzle S(100) (Fig. 7) in comparison with S(50) (Fig. 2 *b* and 3 *a*).

We also calculated the acceleration of copper nanoparticles in micronozzle S(200). All linear dimensions in micronozzle S(200) were twice increased in comparison with micronozzle S(100). The nozzle outlet diameter in micronozzle S(200) was 200 μm, and the nozzle length was 4 mm. The gas and particle quantities at the inlet to micronozzle S(200) had the same values as the quantities in micronozzle S(100) except for the particle diameter, which was increased two-fold, d_p = 200 nm. The calculated impact velocity of the nanoparticles with nm is 590 m/s.

The gas and particle velocities in micronozzles S(50), S(100), and S(200) calculated at constant diameter ratio $D / d_p = 10^3$ are shown in Fig. 9.

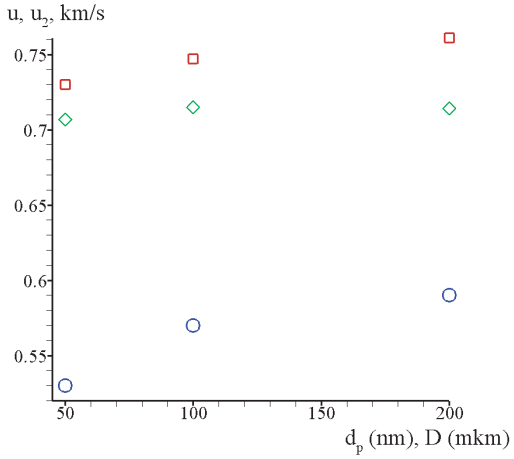

Fig. 9. Gas velocity and particle velocity at the nozzle exit (rectangles and rhombuses, respectively), and the impact velocity of nanoparticles (circles).

It is seen that the gas velocity $u(Z_b)$ and the particle velocity $u_2(Z_b)$ at the nozzle exit plane slightly increase with increasing the micronozzle size. The increase of gas velocity and nanoparticle velocity with increasing the micronozzle diameter D is insignificant, resulting just from the increase of the jet Reynolds number $\mathrm{Re} = u \cdot D / \nu$. In the Navier - Stokes equation written in dimensionless form, the Reynolds number enters the viscous term in the denominator [3]: $\frac{d\vec{v}}{dt} = -\nabla p + \frac{1}{\mathrm{Re}}\Delta\vec{v}$. That is why an increase in the Reynolds number causes a reduction of the viscous friction force and, with it, leads to increasing gas velocity.

Let us examine in more detail now the variation of the impact velocity u_2^* with the diameters D and d_p (Fig. 9). With increasing the diameters D and d_p, the impact velocity u_2^* grows in value much stronger than the particle velocity at the nozzle exit plane. The two-phase jet flow in between the nozzle exit and the obstacle can be analyzed individually in the regions in front of and behind the shock wave.

In front of the shock wave the gas velocity and the particle velocity remain roughly unchanged. Behind the shock wave, in the compression layer, the gas velocity vanishes at the wall. Because of the deceleration in the compression layer, the impact velocity of nanoparticles u_2^* will be lower than the velocity of nanoparticles at the nozzle exit plane $u_{2b} = u_2\,(Z_b)$.

On the assumption that the average gas velocity in the compression layer is of order $u \approx 200$ m/s (Fig. 5 *c*), so that $u - u_{2b} \approx 300$ m/s, we can evaluate the suppression of particle velocity in the compression layer. To this end, from system (2) we derive formulas for the drag force $f_z = (u - u_2) / \tau$, the relaxation time $\tau \approx \rho_p d_p / (3C_d \rho\,(u - u_2))$, and the particle velocity $du_2 / dt = f_z$, and then obtain from these formulas an estimate for the charge of particle velocity in the compression layer $\Delta u_2 = u_{2b} - u_2^*$:

$$\Delta u_2 \approx f_z \cdot \frac{\Delta}{u_{2b}} = \left(\frac{3C_d \rho (u - u_{2b})^2}{\rho_p u_{2b}} \right) \cdot \frac{\Delta}{d_p} \cdot$$

Numerical estimates show the compression-layer thickness to be roughly equal to a quarter of the nozzle outlet diameter $\Delta \approx D / 4$. Since in the calculations performed for micronozzles S(50), S(100), and S(200) the ratio $D / d_p = 10^3$ was kept constant, then the velocity difference can be expected to vary in proportion to the drag coefficient

$$\Delta u_2 \approx \frac{3 \cdot 10^3 C_d \rho (u - u_{2b})^2}{4 \rho_p u_{2b}} \cdot \qquad (4)$$

On substitution of $M_{12} \approx 0.4$ into formula (3), we obtain the drag coefficient values in the compression layer for the various particle diameters: $C_d \approx 12$ for $d_p = 50$ nm, $C_d \approx 9.3$ for $d_p = 100$ nm, and $C_d \approx 6.56$ for $d_p = 200$ nm. With the calculated values of $C_d\,(d_p)$, formula (4) yields: $\Delta u_2\,(50) / \Delta u_2\,(200) = 1.83$ and $\Delta u_2\,(50) / \Delta u_2\,(100) = 1.3$. The particle deceleration values $\delta u_2 = u_{2b} - u_2^*$ obtained for the nanoparticles of various sizes in the numerical calculations for micronozzles S(50), S(100), and S(200) can be taken from Fig. 9: $\delta u_2\,(50) / \delta u_2\,(200) = 1.46$ and $\delta u_2\,(50) / \delta u_2\,(100) = 1.26$. Comparison of these values shows that formula (4) adequately predicts the change of particle velocity in the compression layer versus the particle diameter. It follows from here that the dependence of particle impact velocity on the problem geometry (size effect) is related with the fact that a characteristic relaxation time is involved in equation system (2). System (1, 2) is an equation system non-invariant with respect to the dilation group (scale transformation group) [10], and the solutions of these system are therefore also functions non-invariant with respect to this group.

4. CONCLUSION

In the present study, the possibility of acceleration of copper nanoparticles in a Laval micronozzle to impact velocities sufficient for the formation of a coating on the obstacle surface has been demonstrated. A decrease in the size of nanoparticles impinging onto the obstacle surface necessitates a certain reduction of dimensions of the micronozzle used for particle acceleration. A size effect manifested as the dependence of the impact velocity of nanoparticles on the nanoparticle size was revealed. It is shown that the effect results from the influence which the particle relaxation time has on the process of particle deceleration in the compression layer near the obstacle.

This work was supported in part by the Russian Foundation for Basic Research (Grant No. 08-01-00108-a).

REFERENCES

1. Papyrin A., Kosarev V., Klinkov S., et al. *Cold spray technology*. Elsevier, Amsterdam, 2007.
2. Kiselev S.P., Kiselev V.P., Klinkov S.V., Koserev V.F. Numerical modeling of microparticle acceleration in a Laval nozzle with subsequent deceleration in a wall compression layer. 14-th Intern. Conf. on the Methods of Aerophys. Research (in Russian): Proc. Pt 2., June 30 - July 6, Novosibirsk, 2008.

3. Landau L.D., Lifshitz E.M. *Hydrodynamics (in Russian)*, Nauka, Moscow, 1986.
4. Kiselev S.P., Vorozhtsov E.V., Fomin V.M. *Foundations of Fluid Mechanics with Applications: Problem Solving Using Mathematica*. Birkhauser, Boston-Basel-Berlin, 1999.
5. Boiko V.M., Kiselev V.P., Kiselev S.P., et al. *Shock wave interaction with a cloud of particles*, Shock Waves, 1997,V. 7, P. 275 - 285.
6. Kiselev V.P., Kiselev S.P., Vorozhtsov E.V. *Interaction of a shock wave with a particle cloud of finite size*, Shock Wave, 2006, V. 16, P. 53 - 64.
7. Henderson C. B. *Drag coefficient of spheres in continuum and rarefied flows*, AIAA Journal, 1976, V. 14, No. 6, P. 707 - 708.
8. Rusanov V.V. *Difference schemes of third - order accuracy for shock - capturing computation of discontinuous solutions*, Dokl. Akad. Nauk SSSR (in Russian) 1968, V. 180, P. 1303 - 1305.
9. Anderson D.A., Tannehill J.C., Pletcher R.H. *Computional Fluid Mechanics and Heat Transfer*, Hemisphere Publishing Corporation, 1984.
10. Birkhoff G. *Hydrodynamics. A Study in Logic, Fact and Similitude*, Princeton University Press, Princeton, 1960.